# Fusion of MISR Stereo Cloud Heights and Terra-MODIS Thermal Infrared Radiances to Estimate Multi-layered Cloud Properties

**Arka Mitra[1], Jesse Ray Loveridge[1] and Larry Di Girolamo[1]**

*1. Department of Atmospheric Sciences, University of Illinois at Urbana-Champaign, Urbana, IL*

Corresponding Author: Arka Mitra (mitraarka27@gmail.com)

**Key Points:**

1. Accurate, high-precision MISR low cloud heights are employed in a physics-based correction to MODIS $CO_2$-slicing in multi-layered scenes.
2. Cloud-top pressure bias drops from 65 hPa to 5 hPa, resulting in a quartering of cloud-height and emissivity bias for cirrus over low cloud.
3. Up to 88% of cloud-top pressure retrieval errors are bound by theoretical estimates, resulting in near-closure of $CO_2$-slicing error budget.

## *Abstract*

Our longest, stable record of cloud-top pressure (CTP) and cloud-top height (CTH) are derived from the Moderate Resolution Imaging Spectroradiometer (MODIS) and Multi-Angle Imaging Spectroradiometer (MISR) on Terra. Because of single cloud-layer assumptions in their standard algorithms, they provide only single CTP/CTH retrievals in multi-layered situations. In the predominant multi-layered regime of thin cirrus over low clouds, MODIS significantly overestimates cirrus CTP and emissivity, while MISR accurately retrieves low-cloud CTH. Utilizing these complementary capabilities, we develop a retrieval algorithm for accurately determining both-layer CTP and cirrus emissivity for such 2-layered clouds, by applying the MISR low-cloud CTH as a boundary condition to a modified MODIS $CO_2$-slicing retrieval.

We evaluate our 2-layered retrievals against collocated Cloud-Aerosol Transport System (CATS) lidar observations. Relative to CATS, the mean bias of the upper cloud CTP and emissivity are reduced by ~90% and ~75% respectively in the new technique, compared to standard MODIS products. We develop an error model for the 2-layered retrieval accounting for systematic and random errors. We find up to 88% of all residuals lie within modeled 95% confidence intervals, indicating a near-closure of error budget. This reduction in error leads to a reduction in modeled atmospheric longwave radiative flux biases ranging between 5-40 $Wm^{-2}$, depending on the position and optical properties of the layers. Given this large radiative impact, we recommend that the pixel-level 2-layered MODIS+MISR fusion algorithm be applied over the entire MISR swath for the 22-year Terra record, leading to a first-of-its-kind 2-layered cloud climatology from Terra's morning orbit.

## *Plain Language Abstract*

Our longest climate-quality record of global cloud-top heights (CTH) comes from the Moderate Resolution Imaging Spectroradiometer (MODIS) and Multi-Angle Imaging Spectroradiometer (MISR) on the Terra satellite. These sensors assume a single cloud-layer in retrieving CTH, even though ~30% of global cloud cover is multi-layered. Multi-layered clouds predominantly consist of thin ice clouds over low clouds. Under such conditions, MISR accurately retrieves low-cloud CTH, while MODIS systematically underestimates upper-cloud-layer CTH. Here, we have developed a 2-layered MODIS+MISR fusion CTH retrieval by using MISR's accurate low-cloud CTH as an input to a modified MODIS algorithm. This algorithm combines the complementary capabilities of MISR and MODIS in distinguishing higher and lower clouds and estimates both-layer cloud heights and high-cloud emissivity.

Through comparisons against coincident Cloud-Aerosol Transport System (CATS) lidar observations, we find that the new algorithm improves the accuracies in retrieved CTH and cloud emissivities by ~75% over standard MODIS products. We further demonstrate significant improvements in estimates of simulated atmospheric longwave radiation from our implementation. Owing to its large radiative impact, we suggest that the pixel-level fusion algorithm be applied to all 22 years of Terra record to facilitate public dissemination of the first 2-layered cloud record from its morning orbit.


# *1. Introduction*

The vertical and horizontal distribution of clouds induces gradients in 3D radiative and latent heating rates (McFarlane et al., 2008; Cesana et al., 2019; Athreyas et al., 2020), affecting atmospheric circulation and precipitation patterns (Li et al., 2015; Voigt et al., 2021). As such, clouds play an important role in the Earth's climate – yet, even after decades of research, they remain the key source of uncertainty in predicting future climate change under any given climate change scenario (Boucher et al., 2013). The cloud component of the uncertainty in climate model predictions arises, in part, from approximate sub-grid parametrization of cloud processes in those models (McFarlane, 2011). The sub-grid scale parameterizations are applied to microphysical (hydrometeor size and content) and macrophysical cloud properties (amount-by-altitude and cloud overlap), which together govern the radiative and hydrological properties of clouds. Accurate satellite records of these micro- and macro-physical properties, and their diurnal to long-term variability, are essential to provide empirical constraints on sub-grid cloud parameterizations and climate predictions (e.g., Zhou et al., 2013; Terai et al., 2016; Mace & Berry, 2017).

Our longest record of cloud properties that are stable over multiple decades (features of a desirable climate record) and from a single satellite platform comes from NASA's flagship Earth Observing System (EOS) mission, Terra. It maintained a stable equator-crossing time (ECT; 10:30 am ± 15 minutes) for >20 years (2000-2022), with remarkable radiometric stability in its instruments. This long-term stability in Terra's ECT makes it a unique climate record, since diurnal variability has not been aliased into the patterns of long-term variability.

Two of the instruments on Terra – the Multiangle Imaging Spectroradiometer (MISR) and the Moderate Resolution Imaging Spectroradiometer (MODIS) – employ independent cloud-top height (CTH) retrieval algorithms. MISR retrieves CTHs through visible-channel stereoscopy (Moroney et al., 2002; Muller et al., 2002; Mueller et al. 2013), whereas MODIS employs infrared (IR) techniques, namely the $CO_2$-slicing and 11μm brightness temperature techniques (Menzel et al., 2008; Baum et al., 2012). Both MODIS and MISR CTH retrieval algorithms assume a single cloud layer in the scene. This assumption is often not met in nature as multi-layered clouds occur frequently, with CALIPSO/CloudSat showing that >30% of all clouds occur under various degrees of overlap (Sassen et al., 2008; Joiner et al., 2010; Yuan & Oreopoulos, 2013; Li et al., 2015; Oreopoulos et al., 2017; Hong & Di Girolamo, 2020). By far the most dominant multi-layered cloud regime is a 2-layered system with thin cirrus overlying water clouds, followed by thin cirrus overlying mixed-phase clouds (Wang & Dessler, 2006; Oreopoulos et al., 2017; Hong and Di Girolamo 2020). Numerous validation studies against ground and space-based active sensors have shown that the presence of optically thin cirrus overlying low clouds leads to the most significant disagreements in retrieved CTH between MISR and MODIS (Naud et al., 2007; Marchand et al., 2010; Mitra et al., 2021), suggestive of the presence of independent information of the upper and lower cloud layers in the two datasets.

The path to improving the Terra record relies on exploiting the distinctiveness of the MODIS and MISR CTH techniques to estimate the properties of multi-layered clouds more accurately, as previously suggested (Naud et al., 2007; Mitra et al., 2021). CTH errors in multi-layered cloud regimes have been comprehensively studied for the Terra MODIS and MISR records by Mitra et al. (2021) using collocated Cloud-Aerosol Transport System (CATS) lidar observations (McGill et al., 2015; Yorks et al., 2016) that operated aboard the International Space Station (ISS) from 2015-2017. Comparison of MODIS Collection 6.1 CTH with CATS showed that the CTHs of thin cirrus in these multi-layered regimes were underestimated by more than 1 km on average. 42% of the MODIS CTH retrievals occurred below the cloud base detected by the lidar in these conditions.

Such biases are common in thermal CTH retrievals and are due to the radiative influence of the lower cloud layer reaching the sensor through the optically thin cirrus at infrared wavelengths. On the other hand, the stereoscopic technique employed by MISR tended to retrieve the height of the lower layer when cirrus visible optical depths were less than ~0.4, and with a high degree of precision and accuracy (-280±300 m). However, MISR failed to detect the higher layer in favor of the lower layer >80% of the time in these multi-layered conditions. This is due to the greater contribution of the optically thicker, more textured low clouds to the overall image texture that is used in stereoscopic retrieval. The distinct error characteristics of MISR and MODIS CTH retrievals indicate that there is information about multi-layering of clouds that can be extracted through fusion of the two retrieval methodologies. Here, we present a retrieval algorithm that makes use of the strengths of MISR's sensitivity to low clouds and MODIS $CO_2$-slicing technique's sensitivity to high clouds to retrieve the coincident heights of up to two cloud layers, which also improves the $CO_2$-slicing technique's estimate of the cirrus emissivity. We carry out a detailed error budget analysis and validate the retrievals using CATS.

The remainder of the paper is organized as follows. Section 2 describes the theoretical underpinnings of the $CO_2$-slicing algorithm for retrieving CTH and emissivity of thin ice clouds, and how it has been updated here to account for the presence of an optically thick low cloud measured by MISR. Section 3 describes the datasets used and the method of implementation of a variant of the MODIS single-layered $CO_2$-slicing, along with the implementation of our 2-layer $CO_2$-slicing technique. Section 4 documents the validation of the 2-layer $CO_2$-slicing against coincident CATS lidar observations, along with an error budget analysis for the same. Since cloud radiative effect depends strongly on cloud overlap (e.g., Li et al., 2011; L'Ecuyer et al., 2019, Kang et al. 2020), Section 5 demonstrates significant improvements in modeled cloud radiative effects when using inputs from the 2-layer algorithm compared to the 1-layer algorithm. Concluding remarks follow in Section 6.

## 2. *Theoretical Foundation*

$CO_2$-slicing (Smith & Platt, 1978; Wielicki & Coakley, 1981), as used in MODIS (Menzel et al., 2008), makes use of the difference of clear- and cloudy-sky radiances from closely separated channels in the 13-15 µm $CO_2$ absorption band, where the emissivity for ice clouds (such as cirrus) remain invariant across wavelengths within the band. Clear-sky radiance are estimated through infrared radiative transfer to account for the radiance reaching MODIS that originates from below thin ice clouds. The spectral clear-sky IR radiance, $I_{cs}$ (neglecting scattering) at wavelength λ, reaching a satellite sensor viewing at nadir over a black surface (for simplicity here) is given by:

$$I_{cs}(\lambda) = \mathcal{T}(\lambda, \mathrm{P_s}) B(\lambda, T(\mathrm{P_s})) - \int_0^{\mathrm{P_s}} B(\lambda, \mathrm{P}) \frac{\mathrm{d}\mathcal{T}(\lambda, T(P))}{\mathrm{dP}} \mathrm{dP} \qquad \dots (1)$$

where, $\mathrm{P_s}$ denotes the surface pressure, $B(\lambda, T)$ denotes the Planck radiance at temperature $T$ and wavelength $\lambda$, with temperature defined as a function of pressure, P. $\mathcal{T}(\lambda, \mathrm{P})$ denotes the atmospheric transmittance between $P$ and the satellite. For a completely opaque cloud covering the instantaneous field of view (IFOV) of the sensor, the effective emissivity, which is the product of cloud fraction ($A_c$) within the IFOV and the cloud layer emissivity ($\epsilon_c$), is unity. In this case, provided the opaque cloud is geometrically infinitesimally thin, the nadir radiance observed by the satellite, $I_c$, is devoid of all emissions from below the cloud-top pressure ($P_c$), and is given by:

$$I_c\,(\lambda, P_c) \;=\; \mathcal{T}(\lambda,\, \mathrm{P_c})B\big(\lambda,\, T(\mathrm{P_c})\big) - \int_0^{\mathrm{P_c}} B(\lambda, \mathrm{P})\,\frac{\mathrm{d}\mathcal{T}\big(\lambda,\, T(P)\big)}{\mathrm{dP}}\,\mathrm{dP} \qquad \ldots (2)$$

In reality, cirrus are often transmissive ($\epsilon_c A_c < 1$). Then, the observed nadir top-of-atmosphere (TOA) radiance is:

$$I(\lambda) \;=\; I_{cs}(\lambda) \;+\; \epsilon_c(\lambda)A_c\,[I_c(\lambda, P_c) \;-\; I_{cs}(\lambda)] \qquad \ldots (3)$$

where, $A_c$ is the cloud fraction, and $\epsilon_c A_c$ is often interchangeably referred to as the effective cloud amount or effective emissivity. As effective emissivity for ice clouds is nearly equal for any two wavelengths (say $\lambda_1$ and $\lambda_2$) in the 15µm $CO_2$-absorption band, we set them equal to each other, which, from Eq. 3, leads to

$$\frac{I(\lambda_1) - I_{cs}(\lambda_1)}{I(\lambda_2) - I_{cs}(\lambda_2)} = \frac{I_c(\lambda_1, P_c) - I_{cs}(\lambda_1)}{I_c(\lambda_2, P_c) - I_{cs}(\lambda_2)} \qquad \ldots (4)$$

Cloudy-sky radiances are calculated for a number of discrete $P_c$ values, and the value of $P_c$ for which the right-hand side (RHS) and the left-hand side (LHS) have the least absolute difference is taken as the retrieved $P_c$. Using this value of $P_c$, we can solve for the cloud effective emissivity from Eq. 3, for either band, by:

$$\epsilon_c(\lambda)A_c = \frac{I(\lambda) - I_{cs}(\lambda)}{I_c(\lambda, P_c) - I_{cs}(\lambda)} \qquad \ldots (5)$$

For a 2-layer cloud system, with lower altitude cloud at $P_l$ of effective amount $\epsilon_l(\lambda)A_l$ and an upper altitude cloud at $P_u$ of effective amount $\epsilon_u(\lambda)A_u$, Eq. 3 misrepresents the observed TOA IR radiation at the satellite sensor as it does not consider the emission from the lower cloud layer when the upper-layer is thin (i.e., $\epsilon_u(\lambda)A_u < 1$). In reality, for such a 2-layered system, the background emission (equivalent to the clear-cloudy sky radiance difference in a single-layered case) comes not only from the surface but also from the lower-layer, and hence, $I_{cs}(\lambda)$ in Eq. 3 is modified to be $I'_{cs}(\lambda) = \epsilon_l(\lambda)A_l I_c(P_l) + (1 - \epsilon_l(\lambda)A_l)I_{cs}(\lambda)$, and the TOA IR radiance is:

$$\begin{aligned} I'(\lambda) \;=\; I_{cs}(\lambda) + \epsilon_l(\lambda)A_l[1 - \epsilon_u(\lambda)A_u]\int_{P_l}^{P_s} B(\lambda, \mathrm{P})\,\frac{\mathrm{d}\mathcal{T}\big(\lambda,\, T(P)\big)}{\mathrm{dP}}\,\mathrm{dP} \\ + \epsilon_u(\lambda)A_u[I_c(\lambda, P_u) - \; I_{cs}(\lambda)] \qquad \ldots (6) \end{aligned}$$

Since $I'(\lambda)$ is usually less than $I(\lambda)$, the cloudy-clear radiance differences on the LHS of Eq. 4 are typically reduced when a second layer is present. Hence, simply using the single-layer strategy of Eq. 4 results in a CTP solution that is numerically greater than the true $P_u$. Comparing Eq. 3 and Eq. 6, we note that the second term of Eq. 6 must be accounted for in the $CO_2$-slicing of 2-layered clouds, and hence, Equations 4 and 5 must be updated accordingly. Since the number of unknown variables in Eq. 6 would make solving the equation intractable, we make the simplifying assumption that the lower cloud is black [i.e., $\epsilon_l(\lambda)A_l = 1$], and define the following term:

$$\Delta I\,(\lambda) \;=\; \int_{P_l}^{P_s} B(\lambda, \mathrm{P})\,\frac{\mathrm{d}\mathcal{T}\big(\lambda,\, T(P)\big)}{\mathrm{dP}}\,\mathrm{dP} \qquad \ldots (7)$$

As in a 1-layered $CO_2$-slicing, we assume $\epsilon_u^1 A_u^1 = \epsilon_u^1 A_u^1$ (but now strictly for the upper cloud marked by '$u$'). With all these modifications, Eq. 4 for multi-layered cases is recast as:

$$\frac{I(\lambda_1) - I_{cs}(\lambda_1) - \Delta I(\lambda_1)}{I(\lambda_2) - I_{cs}(\lambda_2) - \Delta I(\lambda_2)} = \frac{I(\lambda_1, P_u) - I_{cs}(\lambda_1) - \Delta I(\lambda_1)}{I(\lambda_2, P_u) - I_{cs}(\lambda_2) - \Delta I(\lambda_2)} \quad \dots (8)$$

Similarly, Eq. 5 is adjusted to account for $\Delta I(\lambda)$, and is recast from Eq. 6, as:

$$\epsilon_u(\lambda) A_u = \frac{I(\lambda) - I_{cs}(\lambda) - \Delta I(\lambda)}{I_c(\lambda, P_u) - I_{cs}(\lambda) - \Delta I(\lambda)} \quad \dots (9)$$

## 3. *Methodology*

Section 3.1 briefly describes the datasets used in this study to both implement and validate our $CO_2$-slicing algorithm. Section 3.2 describes the method of implementation of this algorithm.

### *3.1. Data*

The operational MODIS Cloud Top Property algorithm [detailed in the MODIS Algorithm Theoretical Basis Document or ATBD (Menzel et al. 2015)], which produces the 1 km-resolution Collection 6.1 MOD06 product, uses gridded model output from the National Center of Environmental Prediction Global Data Assimilation System (GDAS) (Derber et al., 1991) for temperature and moisture fields and Reynolds Sea Surface Temperatures (Reynolds et al., 2007) to set up the forward model atmosphere. In our implementation, we have instead used gridded ERA5 Reanalysis products (Hersbach et al., 2020) at 0.25º-resolution, at 4 times a day (i.e., 0, 6, 12 and 18 UTC), to do the same. ERA5 is chosen over other reanalyses because it has been demonstrated to compare better against observations than older reanalyses (Tetzner et al., 2019; Tegtmeier et al., 2020), as well as to use its publicly available modeling error estimates for error budget analysis (see Section 4.2). ERA5 temperatures, specific humidity, and geopotential heights from all 37 ERA5 pressure levels are linearly interpolated as a function of the logarithm of pressure to arrive at the atmospheric state for the 101 pressure levels employed by the MOD06 algorithm. Surface pressures, temperatures (2m temperature over land and sea-surface temperature over oceans) and 2m dewpoint temperatures (to calculate surface moisture) are also used from ERA5 reanalysis, 4 times daily, to define surface temperature and near-surface humidity.

Well-mixed and trace gases (except ozone) are taken from standard atmospheric profiles (Northern/Southern Midlatitude Summer/Winter, Tropical) (Anderson et al., 1986); as are temperatures, specific humidity, and geopotential heights in the uppermost reaches of the atmosphere (i.e., pressures < 1 hPa; ERA5 reanalyses are not available at these altitudes). Between April-September, we assume a Northern Midlatitude Summer; while, between October-March, we assume a Northern Midlatitude Winter. The opposite is true for the Southern Hemisphere. The tropical profile remains invariant for all times of the year and is applied between 30ºN-30ºS, whereas the midlatitude profiles are chosen for latitudes poleward of ±30º. From Collection 6 MOD06, ozone profiles are taken from gridded GDAS output; however, for simplicity, we obtained ozone profiles similar to legacy MOD06 products – climatological ozone mixing-ratio profiles were estimated by linear interpolation in latitude and month among model atmospheres (Tropical, Midlatitude Summer/Winter). Surface emissivity is taken from the same global surface emissivity database used in MOD06 (Seemann et al., 2008).

The observed infrared radiances used in Equations 4/5 and 8/9 are taken from the Collection 6.1 MODIS Level 2 geocalibrated radiance product (MOD021KM). Terra MODIS uses Bands 33, 35 and 36 (13.3, 13.9 and 14.2 µm, respectively) for $CO_2$-slicing CTP estimation [Band 34 (13.6 µm), also a $CO_2$ absorption channel, is unused due to high noise]. Hence, the band-pairs 36/35 and 35/33 are used for estimating CTP (Equations 4 and 8). Band 31 (11.2 µm) radiances are used to calculate effective cloud amounts (Equations 5 and 9).

The low-cloud pressure, $P_l$, is taken from MISR Level 2 CTH (in pressure coordinates). We use the 1.1 km-resolution MISR "wind-corrected" cloud height, from the TC_CLOUD Version F01_0001 product. The low cloud CTH is transformed to pressure coordinates through a linear interpolation between multi-level ERA5 geopotential height and the logarithm of pressure. MISR CTH is reported on the 1984 World Geodetic System (WGS84) ellipsoid, and hence, 0.25º-resolution nearest neighbor geoid heights were added to MISR CTH to obtain low cloud heights above mean sea level, before calculating CTP from it.

We validate our $CO_2$-slicing technique by comparing against coincident observations from the CATS lidar. Thus, our validation is restricted to latitudes traversed by the ISS orbit (±52º in either hemisphere). The CATS data is taken from the CATS Version 2.01 Level 2 Product, that reports lidar observations such as 1064 nm cloud-masked lidar backscatter at an along-track resolution of 5 km and a vertical resolution of 60 m. We use the same dataset of CATS CTH, layer depth and layer-integrated backscatter used in Mitra et al. (2021) for this study. As in Mitra et al. (2021), CATS, MISR and MODIS samples were selected only if they are collocated (< 1 km) and coincident (< 5 minutes), for robust statistical analysis. Note that the filtering of multi-layered scenes in our study must be based solely on MISR and MODIS retrievals. Based on the discussion in Section 2, our algorithm is best suited for scenes with a thin ice-phase cloud overlying a vertically well-separated low cloud layer (further discussed in Section 3.2). To ensure application only on ice-phase clouds, we apply our algorithm only on scenes where the MOD06 product had used $CO_2$-slicing for cloud-top detection (since $CO_2$-slicing is only applied on ice-phase clouds). To ensure that our algorithm is applied on scenes with well-separated cloud layers, we choose only those scenes where MODIS-MISR CTH difference > 1 km [suggestive of well-separated cloud layers, based on Mitra et., al (2021)]. Upon imposing these conditions, it is found that all scenes in the remaining dataset are indeed multi-layered according to CATS. 95% are likely 2-layered (for 92% of such cases, the CATS signal completely attenuates in the second layer). The remaining 5% pixels show attenuation in a third cloud layer. The final dataset constitutes 2790 pixels from 501 independent scenes (i.e., unique MISR and MODIS granules and CATS orbits), hence ~6 samples per scene (Figure S1). Out of these, 305 (~11%) pixels are no-retrievals. This is largely due to the presence of radiance artifacts, such as striping within the MODIS data. In the current study, such bad pixels are discarded from the analyses, but can be dealt with in future implementations by established procedures of MODIS radiance de-striping (Weinreb et al., 1989; Bouali & Ladjal, 2011).

IR emissivity ($\epsilon_{IR}$) of a cloud layer is related to visible optical depth ($\tau_{VIS}$) over the layer, as

$$\tau_{VIS} = -\zeta \ln(1-\epsilon_{IR}) \qquad \ldots (10)$$

where, $-\ln(1-\epsilon_{IR})$ equals the thermal IR optical depth ($\tau_{IR}$). The constant $\zeta$ is taken to be 2.13 for ice clouds (Minnis et al., 1993; Rossow & Schiffer 1999). Estimates of visible optical depth

($\tau_{VIS}$) of the topmost cloud layer from CATS comes from a linear regression between layer-averaged integrated backscatter and layer-integrated optical depth for high clouds (CTH > 7 km) [detailed in (Mitra et al., 2021)]. These estimates of high cloud $\tau_{VIS}$ are converted to infrared effective emissivity ($A_c\epsilon_c$, assuming $A_c$ = 1) using Eq. 10 for validation. MODIS 1 km-resolution CTP, CTH, effective emissivity ($A_c\epsilon_c$) and visible optical depth ($\tau_{VIS}$) from the MOD06 product are also used in comparison to CATS and our 2-layered solution.

### *3.2. Implementation of the $CO_2$-slicing Algorithm*

For our implementation of the $CO_2$-slicing algorithm, we have modified the original MOD06 Fortran Cloud-Top Property code obtained from the MODIS Adaptive Processing System (see Section 7) and wrapped it in Python. Salient features of the operational code and the modifications for our implementation are hereby discussed.

The MOD06 algorithm simulates clear- and cloudy-sky radiances using Equations 1 and 2, on 101 vertical pressure levels between 0.05 to 1100 hPa, taking gaseous absorption, surface emissivity and satellite zenith angle into account. These radiances are calculated for the channels centered on 11.2, 13.3, 13.6, 13.9 and 14.2 µm, using a transmittance model named Pressure layer Fast Algorithm for Atmospheric Transmissions (PFAAST) (Hannon et al., 1996), and further corrected for increased path-length along off-nadir viewing zenith angles. The usage of these modeled radiances along with the observed radiances from MODIS, in Eq. 4, requires that the cloud emissivity for pairs in the $CO_2$-slicing spectral bands be nearly equal, which is more satisfied by ice clouds than water or mixed-phase (Zhang & Menzel, 2002). Hence in generating the standard MOD06 product, the MODIS cloud phase detection algorithm is run ahead of the cloud-top algorithm. The $CO_2$-slicing technique is applied only on such scenes with ice phase detection (11.2 µm brightness temperature technique is applied elsewhere).

In our implementation we use the same PFAAST model and we account for cloud phase by selectively working only on those pixels where the Collection 6.1 MODIS $CO_2$-slicing had been previously used. Global comparison of Aqua-MODIS cloud phase with CLOUDSAT-CALIPSO data had shown that the MODIS cloud phase algorithm mischaracterizes multi-layered clouds with an upper ice layer as liquid or mixed in <1% of all cases (Marchant et al., 2016). This ensures confidence that pixels flagged as confidently ice by the Terra MODIS cloud phase algorithm is nearly always ice topped and hence, suitable for the implementation of our algorithm.

#### *3.2.1. Implementation of a Single-layered $CO_2$-slicing and its Bias*

To obtain solutions for CTP and emissivity, Eq. 4 is solved iteratively between the surface and the tropopause, to obtain the value of $P_c$ that best reduces the difference between LHS and RHS of Eq.4. The tropopause is chosen as the upper limit of CTP solution, because the temperature profile is nearly flat across the tropopause, leading to non-unique solutions. The tropopause is taken to be the level of the highest altitude inflection point in the reanalysis temperature profile for pressures > 100 hPa. If many points satisfy such a condition, the lowest altitude point is chosen to be the tropopause. The solution of $P_c$ from Eq. 4 is then used in Eq. 5 using 11.2 µm radiances to estimate effective cloud amounts ($A_c\epsilon_c$).

The standard MOD06 algorithm calculates all possible CTP solutions, before only reporting a “best” solution through a “top-down” method that checks for the possibility of a higher wavelength solution before a lower wavelength or brightness temperature solution (i.e., 36/35 solution over

35/33 solution, over an IR BT solution) (Menzel et al., 2008). For a solution to be viable, the clear-cloudy radiance difference must exceed noise levels for each particular channel in that spectral band pair (designated to be 1.25, 1.0, 1.0 and 0.75 W m$^{-2}$ sr$^{-1}$ for Bands 36-33, respectively), and the solution from that channel must lie within a specific portion of the troposphere where the atmosphere is emissive for that spectral channel (i.e., for 36/35 pair, CTP solutions must be < 450 hPa; for the 35/33 pair, CTP solutions must be < 650 hPa) (Baum et al., 2012).

To verify the implementation of our algorithm, we compared our 1-layer CTP solutions against MOD06 CTP for 500 CATS single-layer high cloud (CTH > 7 km) pixels from 42 independent scenes in January-February 2016. We find a mean (± standard deviation) difference in CTP between our implementation and MOD06 to be -5±30 hPa. For these scenes, the mean CTP bias (relative to CATS) for MOD06 is 20±30 hPa, whereas it is 15±35 hPa for our implementation. This provides confidence in our implementation, while also underscoring the fact that moving from GDAS to ERA5 reanalysis had only a minor impact on the single-layer $CO_2$-slicing retrieval.

To estimate the systematic errors accrued from cloud overlap in $CO_2$-sliced CTP, we conduct an experiment where we apply the 1-layered $CO_2$-slicing on 2-layered cloud systems. For these experiments, we employ the forward model described in Section 3.2 to calculate synthetic radiances for the 2-layered system, except we include a lower, black cloud layer as in Eq. 6. We then use Equations 4 and 5 to retrieve the CTP under the assumption of a single layer and examine the resulting errors. This experiment is idealized in that it neglects any errors in the forward model. We perform retrievals on the synthetic two-layered systems for a climatological tropical atmosphere for different values of $P_u$ and $P_l$. We calculate the overestimations of CTP above $P_u$ for four effective cloud amounts between 0.05-0.75 and for each of the spectral band pairs that are used by Terra MODIS, with results shown in Fig. 1. Here we see that the highest overestimation of high-cloud CTP (i.e., an underestimation of high-cloud CTH) occurs in the 35/33 band pair for a combination of very thin high cirrus over a low cloud (provided the low cloud is sufficiently decoupled from the surface). It is unsurprising that the 35/33 band pair is more susceptible to the presence of low clouds, because there is a large reduction in the amount of near-surface radiation that reaches the satellite sensor in going from 13.3 to 14.2 μm due to increasing absorption by $CO_2$. For the same high-low cloud combination and same spectral band pair, it is also unsurprising that the thinnest of clouds ($\epsilon_c\ A_c$ = 0.05) has the highest errors in CTP determination. As the lower cloud approaches either the high cloud or the surface, the 2-layered system essentially becomes indistinguishable from a single-layered high cloud; hence, in both these extreme conditions, the bias is reduced. These results are similar to the estimates of CTP bias arising from the application of a 1-layered $CO_2$-slicing for 2-layered cloud systems by the HIRS/2 sounder (Figures 3, 5 and 6 in Baum & Wielicki, 1994) and MODIS (Figure 10a of Menzel et al, 2015).

Based on these findings, our bias-correction approach (Equations 8 and 9) for two-layered cloud systems will have the largest correction for well-separated cloud layers, particularly when the lower cloud-top is both sufficiently colder than the surface and warmer than the upper-layer cloud.

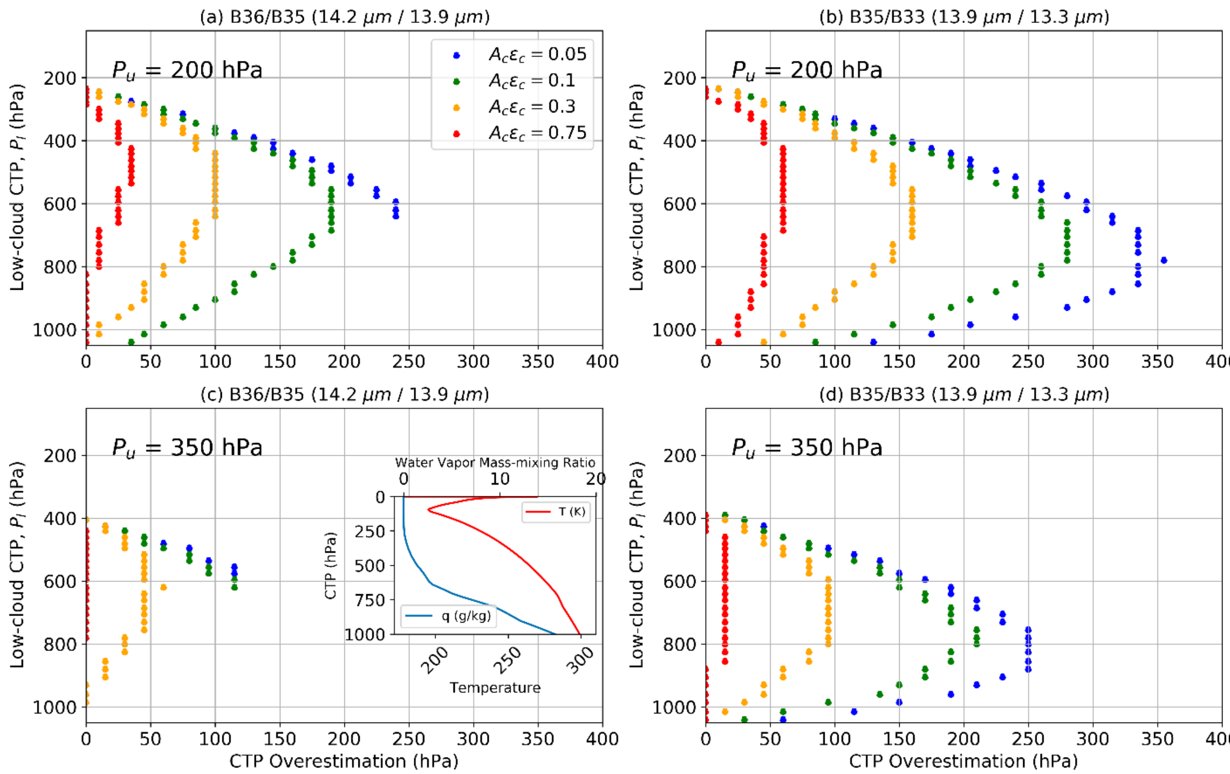


*Figure 1. Bias in CTP from MODIS CO2-slicing (under single-layer assumption) for Bands 36/35 (left panels) and 35/33 (right panels) for a high cloud at pressure = 200 hPa (upper panels) and 350 hPa (bottom panels), given a standard tropical atmosphere profile of water vapor (g/kg) and temperature (K; inset in c). Climatological profiles of ozone and trace gases are used. The lower cloud is assumed opaque, and the surface (1014 hPa) is a dark ocean. For each high-low combination, the experiment is repeated for cloud emissivities of 0.05 (blue), 0.1 (green), 0.3 (orange) and 0.75 (red).*

#### ***3.2.2. Implementation of the 2-layered $CO_2$-slicing***

The modification to the $CO_2$-slicing solution for a 2-layered system involves replacing Equations 4 and 5 with Equations 8 and 9 in the $CO_2$-slicing workflow, which, in turn, requires the computation of the term $\Delta I$, given by Eq. 7. This step requires the value of MISR CTP (Section 3.1). The closest of the 101 MODIS levels to MISR CTP is taken as $P_l$ in Eq. 7. Solutions for $P_u$ from band pairs 36/35 and 35/33 are recorded. A best solution is also chosen using the "top-down" method. If no legitimate solution is found (Section 3.2.1), it is a no-retrieval.

All 2485 valid CTP retrievals are converted to CTHs, using ERA5 geopotential heights. All such retrievals are also used to estimate effective cloud amounts (using Eq. 9). MOD06 effective cloud amounts are also used for comparison. Following Eq. 10, effective cloud amounts are converted to visible optical depths ($\tau_{VIS}$), assuming $A_c = 1$. Note, the estimates for $A_c\epsilon_c$ and $\tau_{VIS}$ are estimates of the high cloud optical properties retrieved after the radiative contribution of the lower cloud has been removed. In contrast, the corresponding MOD06 retrievals are effective estimates of those quantities retrieved using the combined radiation from both upper and lower cloud layers.

This aforementioned modification to the $CO_2$-slicing is rooted in physical theory and makes use of Terra's unique design for fusion between instruments, which allows us to improve the MODIS upper-layer CTP/CTH and emissivity, provided the layer is optically thin for MISR to retrieve

CTH of the lower cloud [this is also the regime where MODIS $CO_2$-slicing CTH errors are maximum (Mitra et al., 2021)]. To distinguish the new high cloud properties from the operational MODIS data variables, we shall refer to the new estimates of cirrus CTP/CTH, $A_c\epsilon_c$ and $\tau_{VIS}$ as the *MISR-MODIS Fusion Product for Cloud-Top Height* (MM_CTH).

## 4. *Validation*

In Section 4.1, MM_CTH and MOD06 estimates of high cloud macrophysics and optical properties will be validated against CATS estimates of those quantities. Section 4.2 provides a detailed error budget analysis of our 2-layered $CO_2$-slicing CTH retrieval with the goal of closing the total error budget had through a comparison with CATS CTH.

### *4.1. Comparison with the CATS lidar*

To validate our new algorithm, we compare the results of high cloud CTP/CTH, high cloud effective emissivity ($A_c\epsilon_c$) and visible optical depths ($\tau_{VIS}$) from MM_CTH against concurrent MOD06 and CATS observations. We divide the validation of MM_CTH along two lines – validation of high cloud macrophysics (CTP, CTH) and high cloud optical properties ($A_c\epsilon_c$, $\tau_{vis}$).

#### *4.1.1. Validation of High-Cloud Macrophysical Properties*

As in Mitra et al. (2021), we take CATS CTH/CTP to be an unbiased truth in our analysis. CATS CTH is converted to CATS CTP, using ERA5 geopotential and standard geoid heights, in the same manner as MISR CTH to CTP conversion. Figure 2 shows the distribution of CTP/CTH differences between $CO_2$-slicing techniques (MOD06 and MM_CTH) and the lidar on the left panels, and the distributions of high cloud CTP/CTH from the 3 techniques (MOD06, MM_CTH and CATS) on the right panels. The mean bias (±standard deviation) in retrieved CTP and CTH improves from 65±85 hPa and -1.6±2.3 km, respectively, for MOD06 to 5±80 hPa and -0.4±2.4 km for MM_CTH. This represents a ~90% reduction in CTP bias and a ~75% reduction in CTH bias.

The reduction in the CTP/CTH bias for high-cloud retrievals results in improved high cloud macrophysical distributions (right panels of Figure 2), with the MM_CTH distributions of CTP/CTH closely mirroring those from CATS. Mitra et al. (2021) showed that for 42% of all scenes with a thin cirrus overlying a low cloud, MODIS CTH lies below the vertical extent of the cirrus (i.e., lower than CATS cloud-layer base). The application of the 2-layered MM_CTH reduces the instances of such below-cloud-base height retrievals to 12%.

For the distributions of MM_CTH minus CATS CTP and CTH (Figures 2a and 2c), we note the existence of a significant number of scenes (~4% of each distribution) where MM_CTH appears to overestimate the value of CATS CTH by > 4 km (i.e., underestimate CTP > 100 hPa). Previous studies (Rajapakshe et al., 2017; Mitra et al., 2021) had identified these as scenes where the 1 km-resolution infrared sensor detects physically tenuous (e.g., broken cirrus) clouds, but the lidar's 5 km-resolution algorithm picks the height of a lower, possibly horizontally continuous, cloud field. Here, we show that this assertion is indeed true by calculating the mean MISR-CATS CTH for scenes with MM_CTH – CATS CTH difference > 4 km, and finding a mean difference of -0.5±0.5 km. This is close to MISR's CTH accuracy for low clouds (Mitra et al., 2021). Thus, in these scenes, MODIS retrieved cirrus heights and CATS retrieved low cloud heights. Such an effect is noticeably smaller in the corresponding MOD06 distributions because MOD06 estimates of CTH (CTP) are lower (higher), and hence, closer to the CATS low-cloud retrievals.

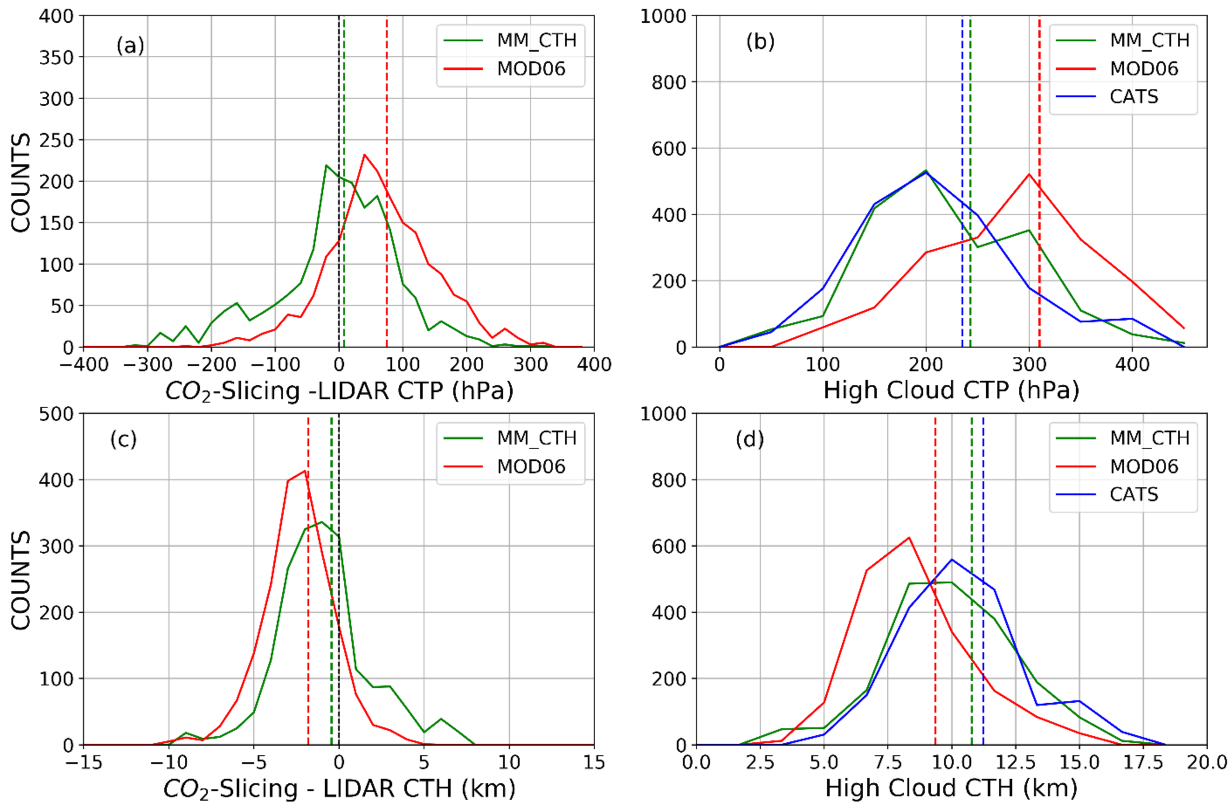


*Figure 2. Distribution of errors (left) in CTP (top panels; hPa) and CTH (bottom panels; km) from MOD06 (red) and MM_CTH (green) and the distribution of high cloud macrophysics (right panels) for multi-layered scenes from MOD06 (red), MM_CTH (green) and CATS (blue). The vertical dashed lines in each color represents the mean value of the quantities whose distributions are in that same color.*

### *4.1.2. Validation of High-Cloud Optical Properties*

Unlike cloud-top properties (CTP and CTH), we do not have an unbiased estimate for cloud effective amount ($A_c\epsilon_c$). As a result, we have converted CATS $\tau_{VIS}$ to CATS $A_c\epsilon_c$ by inverting Eq. 10 (taking $\zeta = 2.13$ and assuming $A_c = 1$). Even though this is not an unbiased estimate of true $A_c\epsilon_c$, one can reasonably expect the CATS $A_c\epsilon_c$ to be a closer estimate of true cirrus emissivity as compared to MOD06 $A_c\epsilon_c$, because the MOD06 $A_c\epsilon_c$ estimate is impacted by the lower cloud layer. As shown in Figure 3, we have compared MM_CTH estimates of $A_c\epsilon_c$ and $\tau_{VIS}$ against CATS and MOD06 estimates of those quantities. The improvements in cloud macrophysical retrievals shown in Section 4.1.1 have propagated to improvements in retrievals of high cloud optical properties. From Fig. 3, we notice a ~75% increase in accuracy in both $A_c\epsilon_c$ and $\tau_{VIS}$ for MM_CTH over MOD06 (assuming that CATS emissivity and $\tau_{VIS}$ are unbiased). These improvements lead to MM_CTH distributions of high cloud emissivity and optical depths that are comparable to the corresponding distributions from the CATS lidar.

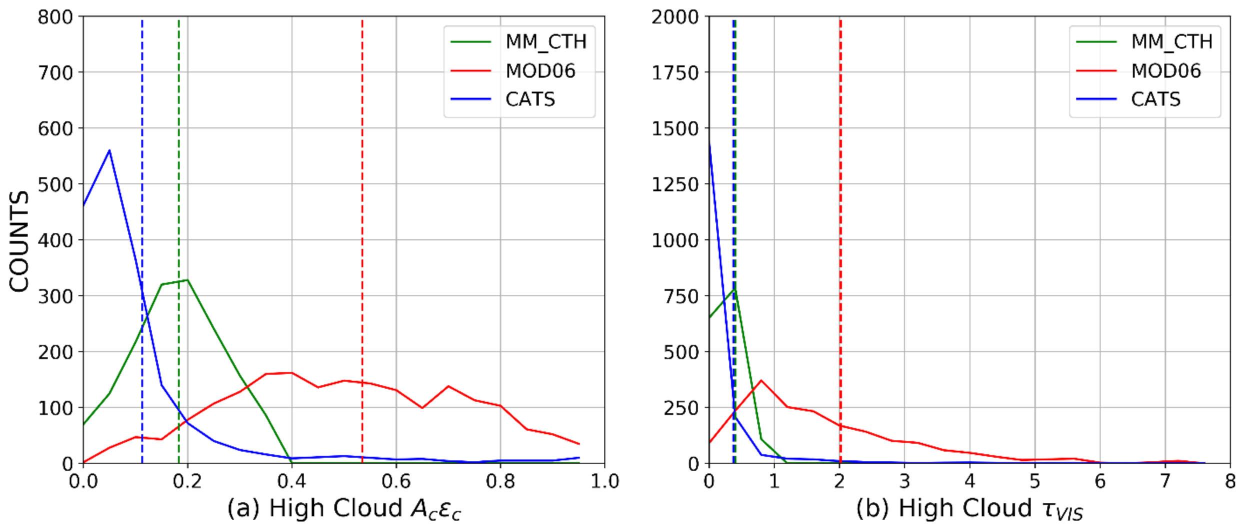


*Figure 3. Distribution of effective emissivity (left) and visible optical depth (right) from MOD06 (red), MM_CT (green) and CATS (blue) for high clouds in multi-layered scenes. The dashed lines in each color represents the mean value of the quantities whose distributions are in that same color. On the right plot, the mean values of $\tau_{vis}$ from MM_CTH and CATS are visibly indistinguishable.*

The MOD06 estimates of $A_c\epsilon_c$ and $\tau_{VIS}$ are both overestimations of true high-cloud optical properties because their individual retrieval methods do not remove the radiative contribution of the lower cloud. As a result, both are effective retrievals over all cloud layers. Improved estimates of upper-cloud optical properties (especially $\tau_{VIS}$) are crucial in the accurate representation and tuning of cloud radiative effects in models (which we demonstrate in Section 5). In Fig 4b, the MOD06 estimates of $\tau_{VIS}$ are from the standard MODIS bispectral optical depth retrievals (Platnick et al., 2017) which use visible channel radiances and separate pre-computed look-up tables for ice and water clouds. As such, since we are working on scenes where MODIS cloud phase detected ice, the ice look-up tables had been used to retrieve $\tau_{VIS}$ for a 2-layered multi-phase system. Here, we have improved the retrieval by improving our estimates of only the cirrus $\tau_{VIS}$. However, with the improvements achieved by MM_CTH in defining the CTP of the ice and water cloud layers, future work can design 2-layered ice + water/mixed phase cloud look-up tables to simultaneously retrieve the visible optical depths of both cloud layers present within the scene.

In the previous sections, we have presented the validation of MM_CTH retrievals against CATS lidar. A detailed discussion of the CTP error budget follows in Section 4.2.

### *4.2. The 2-layered $CO_2$-slicing Error Budget Analysis*

In this section, we shall investigate the effect of various sources of systematic and random errors on MM_CTH CTP with the goal of comparing the total computed error against those shown in Section 4.1 (note that we do not repeat this exercise for effective emissivity as we do not have a truth dataset for that quantity). We consider the following sources of errors:

i. the uncertainty in MISR low-cloud stereo heights,
ii. the covariance of modelling errors in ERA5 Reanalysis temperature and specific humidity,
iii. the inherent noise in detected radiances from the MODIS spectral bands,
iv. the effect of geometric depth of cirrus clouds,
v. the uncertainty in the geo-collocation of CATS, MISR and MODIS pixels,
vi. the uncertainty incurred from the application of spatial interpolation to obtain atmospheric parameters at the 101 MOD06 vertical pressure levels,
vii. the breakdown of the assumption that the low clouds are perfectly black, and
viii. the effect of uncertainty in surface emissivity.

Empirical error estimates are known (as explained below) for the first six items on the list above. However, we lack a 'truth' dataset for low cloud opacity and surface emissivity. Hence, error sources vii and viii will be dealt with in a different manner to the others.

We run radiative transfer simulations over a range of 2-layered cloud combinations and use the simulated radiances in MM_CTH retrievals to estimate CTP errors. We compile these errors, $E$ (bias and standard deviation), in the prescribed functional form: $E = E(P_{high}, depth, \tau_{VIS}, P_{low}, \lambda_{pair}, climate\ zone)$. Here, $P_{high}$, $depth, \tau_{VIS}$ are CTP, geometric depth, and visible optical thickness of the high clouds in the simulations. $P_{low}$ is the CTP of the low black cloud. $\lambda_{pair}$ refers to the MODIS band-pair being employed (i.e., either 35/33 or 36/35), and $climate\ zone$ denotes the 5 climate zones introduced in Section 3.1. For each climate zone and $\lambda_{pair}$, we run the MM_CTH algorithm for every combination of the following:

(a) 10 values of $P_{high}$ (50 hPa intervals between 150 and 550 hPa)
(b) 6 values of $P_{low}$(50 hPa intervals between 700 and 1000 hPa)
(c) 5 values of geometric depth (25 hPa intervals between 25 and 150 hPa)
(d) 8 values of $\tau_{VIS}$ (0.25 intervals between 0.25 and 2.5)

This leads to 2400 cases for each band-pair and climate zone (hence 24000 in total). We choose the ranges for high cloud properties and $P_{low}$ from the distributions of high cloud properties and low cloud heights (in units of pressure) that we observed in the CATS and MISR data used in this study. Out of the variables on which the error function $E$ depends, we expect there to be significant random variability in estimates of $P_{low}$, ERA5 reanalysis profiles and MODIS infrared radiances (error sources i, ii, and iii). To model this expected variability, we perturb these 3 quantities to derive 200 different realizations of each of the aforementioned 24000 cases. We do this to propagate the uncertainties in these quantities to uncertainties in simulated radiances and thereby, to uncertainties in retrieved CTP. This procedure is detailed below.

**a) Low-cloud CTP:** Mitra et al. (2021) showed that MISR low cloud CTH error is -230±300 m. This error is propagated to CTP error using the formula $\sigma_P = \left|\frac{P}{H}\right| \sigma_z$, where, $\sigma_P$ is the pressure uncertainty at a pressure level $P$ corresponding to a height uncertainty of $\sigma_z$, for a pressure profile that varies with height according to the formula $P(z) = P_o e^{-z/H}$. Here, $P_0$

is the pressure at surface (z = 0), z is the altitude of the pressure level and H is the scale height of the atmosphere, given by the altitude where $P = P_0/e$. For every low-level cloud, we bias our estimate of low-cloud CTP by taking the pressure equivalent of MISR CTH + 230 m (using the form for *P(z)*, given above) and then perturb the resulting $P_{low}$ by drawing 200 different samples drawn from a normal distribution given by $\mu=P_{low}$, $\sigma = \sigma_P$.

b) **ERA5 Reanalysis Error:** To estimate the error-covariances of the ERA5 temperature and moisture profiles, we used the results of all model ensemble (Hersbach et al., 2020) that are publicly available along with ERA5 reanalysis (given by the ensemble mean). These ensemble members provide flow-dependent uncertainties based on propagation of assimilated measurement uncertainties as well as perturbations to physical tendencies. We took data from all grid cells over the globe over a day from each month of 2016 and calculated flow-dependent perturbations by subtracting each ensemble member from the ensemble mean. We then grouped the perturbations by latitude and season in the 5 pre-defined climate regimes (Section 3.1). Here, we estimated the error-correlations between all pressure levels of the profiles of temperature and moisture reanalysis, neglecting error-correlations between adjacent columns. Horizontal error correlations are neglected, as they are only relevant for the aggregation of pixel retrievals, not for individual pixel-level uncertainties. Upon comparing against estimates of ERA5 uncertainty from field studies (Graham et al., 2019), we found that the ERA5 ensemble variance is similar to observed uncertainty for specific humidity profiles. However, the ensemble uncertainty underestimates observed uncertainty of Graham et al. (2019) by a factor ranging between 4-6, depending on pressure level. To correct this discrepancy, temperature profile perturbations from the ERA5 ensemble data are inflated by a constant value of 5, for all pressure levels. For each climate regime, we then propagated the resulting errors to errors in CTP through Monte Carlo sampling. Specifically, we drew 200 perturbed profiles of temperature and specific humidity assuming multivariate Gaussian distributions. The mean value of these distributions are given by their climatological profiles and their covariance matrix is set as described above.

c) **Instrument Noise**: We introduced further perturbations to the calculated TOA radiances, by drawing 200 random samples from a normal distribution with $\mu=0$, $\sigma = 1$ W m$^{-2}$. Here, we have set σ as the mean noise level for the Terra MODIS $CO_2$-slicing channels (as noted in Section 3.2.1, the noise levels in Bands 33-36 varies between 0.75-1.25 Wm$^{-2}$).

To model the error from finite cloud geometric depth (error source iv), we modify the gas-only model (Section 3.2) for clear-sky radiative transfer to include cloud. We prescribe a cloud optical depth, cloud-top and bottom pressure (based on our choices of $P_{high}, P_{low}, depth, \tau_{high}$ listed (a) to (d)). We assume that cloud extinction is homogeneously distributed in pressure over the cloud depth. We verify our implementation using the analytic solution for an isothermal, non-scattering atmosphere. We use this model to simulate radiances in the $CO_2$-slicing bands for geometrically thick, non-black clouds and estimate the CTP retrieval errors stemming from the infinitesimally thin high cloud assumption of the $CO_2$-slicing technique. Gas optics uncertainties are numerically insignificant (<<1% of instrument noise) (Hannon et al., 1996) and are hence, ignored.

With the major sources of systematic and random errors accounted for, we run the MM_CTH algorithm for all 200 perturbed instances of each of the 24000 combinations of

$(P_{high}, P_{low}, depth, \tau_{high}, \lambda_{pair}, climate\ zone)$. We note the bias and standard deviation in CTP for each of those instances to construct the error function, *E* for comparison against observed error.

To account for further sources of random error (error sources v and vi), we estimated the uncertainty in CTP introduced by the process of geo-collocation of MODIS and CATS pixels. Mitra et al. (2021) showed a maximum uncertainty of 900 m in CTH due to the geo-collocation of MODIS and CATS pixels for CATS retrievals above an altitude of 5 km. Using the equation to propagate height errors to pressure errors given earlier, we estimate this collocation uncertainty (given by $\sigma_{coll}$) for all pixels. The errors in interpolating our CTP solutions to the discrete grid employed by the MODIS algorithm also result in an additional source of random error. This error, which we denote by $\sigma_{grid}$ is numerically equal to half the grid-spacing between the nearest two levels of a CTP solution. As in Mitra et al. (2021), the random error in CATS CTH (converted to a CTP error given by $\sigma_{CATS}$) is equal to that associated with an equal probability of successful or failed retrieval over a 60 m CATS range gate, i.e., a random error of 30 m. Since, these sources of error are mutually independent, we estimate total random uncertainty (in a pixel-level retrieval) as $\sigma = \sqrt{\sigma^2_{modelling} + \sigma^2_{coll} + \sigma^2_{grid} + \sigma^2_{CATS}}$ where, $\sigma_{modelling}$ is the error incurred from the various uncertainties in the radiative transfer simulations (sources i to iv), that are accounted by the standard deviation estimates from the error matrices, $E$.

To ascertain the fraction of pixels that are bound by our calculated total error estimates in *E*, we investigated the distribution of bias-corrected errors, normalized by $\sigma$, i.e., $\frac{CTP_{MM} - bias - CTP_{CATS}}{\sigma}$, where $CTP_{MM}$ is the estimated value of CTP from the MM_CTH method, $CTP_{CATS}$ is the observed (also, the assumed "true") CTP from CATS, whereas, *bias* is the closest estimate of theoretical systematic error for a particular pixel from the error matrices, $E(P_{high}, P_{low}, depth, \tau_{high}, \lambda_{pair})$. We find 78% of all pixels to be within the bounds of 95% confidence interval (i.e., [-1.96, 1.96] in units of $\sigma$). The remaining 17% (i.e., 95% minus 78%) of errors remain outside the purview of what can be constrained against empirically observed variables. We suspect that low cloud non-opacity and uncertainty in surface emissivity are the reasons behind these outliers.

We argue that surface emissivity is a less significant source of uncertainty than low clouds because in most multi-layered cases, the surface remains partly to nearly obscured by an opaque low cloud and >70% of all retrievals in our dataset are done by the 36/35 band pair (which is nearly insensitive to surface emissions; Menzel et al., 2015). Moreover, the effect of surface emissivity only becomes relevant in the very cases where the black low cloud assumption breaks down – e.g., for broken low clouds. Hence, we do not investigate surface emissivity separately. To investigate the effects of low-cloud properties, we first note that the non-opacity of low clouds (i.e., $A_l\epsilon_l \neq 1$) may arise due to the presence of sub-pixel low clouds (e.g., small trade wind cumuli) or due to the presence of optically thin low clouds with $\epsilon_c < 1$. To quantify the errors in such scenarios, we relaxed the condition of a low, black cloud by assuming low cloud effective amounts of 0.1 iterations between 0.1-0.9 for each of the 24000 test cases listed above. Effective IR emissivity of the low cloud is then converted to cloud optical depth (using Eq. 10 with $\zeta = 2.56$ for liquid water (Minnis et al. (1993)), and the transmission profile is adjusted accordingly. Surface emissivity is taken to be 1. In spite of the non-black low cloud, we still solve for the high cloud CTP assuming $A_c\epsilon_c = 1$. The mean and standard deviation of the resulting errors over all possible cases, for each value of low-cloud effective amount and MODIS $CO_2$-slicing band pair, are computed and shown in Figure 4. For the Band 36/35 pair, unsurprisingly (since this pair is less sensitive to surface emission), low-cloud semitransparency leads to lower and nearly constant error, irrespective of the low cloud amount (especially, for $A_c\epsilon_c > 0.4$). However, the standard deviations of error for the Band 35/33 pair drops significantly as low cloud amount increases.

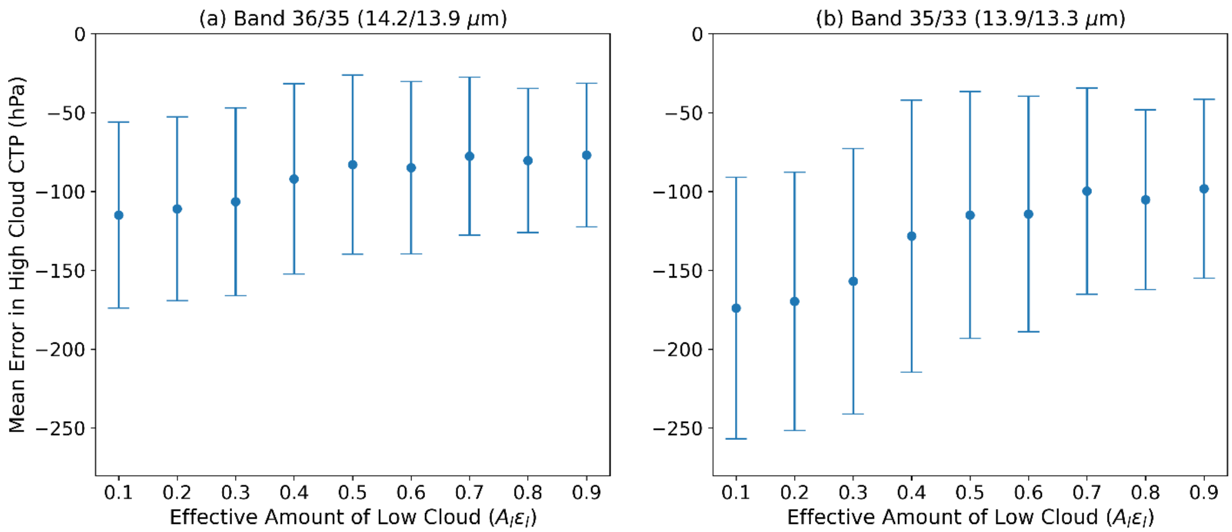


*Figure 4. Distribution of errors in CTP (in hPa) incurred from the breakdown of the assumption of a black low cloud, from MODIS Band Pair 36/35 (left) and 35/33 (right) for different values of thermal IR effective emissivity ($A_c\epsilon_c$) of the low cloud.*

Taking the effect of non-opaque low cloud into account, we redefine the bias-corrected errors to mean $\frac{CTP_{MM} - bias - bias_{low} - CTP_{CATS}}{\sigma}$, where $bias_{low}$ is defined as the mean bias for both band-pairs in Fig 4, weighted by their relative frequency of usage in our dataset. We calculate distributions of bias-corrected error (in units of σ) for all values of $A_l\epsilon_l$ and study the percentage of errors which lie within 95% CI in each case. Taking low clouds into account results in > 80% of all pixels lying within 95% CI for all values of $A_l\epsilon_l$. We find that the maximum agreement between theoretical and observed errors is achieved for $A_l\epsilon_l$ = 0.3, resulting in 88% of all bias-corrected errors within the 95% CI. Here, we note that the expected dominant effect of low-cloud heterogeneity is likely from sub-pixel clouds. Assuming $\epsilon_l = 1$, this would suggest that the average value of low-cloud fraction in our dataset is $A_l = 0.3$. For 1-km resolution MODIS pixels, a low-cloud fraction of 0.3 equals an average area-equivalent diameter for low clouds in our dataset of 620 m. This seems reasonable as our dataset has samples from both trade cumulus regions with typical cloud diameters of ~450 m (Zhao and Di Girolamo, 2007) and from regions with more stratiform clouds (that would typically cover the entire 1 km MODIS pixel). Thus for $A_l\epsilon_l$=0.3, only 7% of all pixels are not constrained by our theoretical estimates (denoted by 95% CI), we can say that a near-closure of the MM_CTH $CO_2$-slicing error budget has been achieved. The sources of error that could potentially explain these outliers are the incomplete modeling of low-cloud uncertainties, uncertainties in surface emissivity, inaccuracies in MODIS cloud phase detection and the assumption in $CO_2$-slicing of equal ice-cloud effective emissivities in closely spaced IR channels.

## 5. *Impact on Cloud Radiative Effect*

As noted in Section 1, the vertical distribution of cloud properties controls the vertical variation of cloud radiative effect (CRE), defined here as the difference in upwelling cloudy and clear sky radiative fluxes at the top of the atmosphere (and similarly for downwelling radiative fluxes at the surface). When high and low clouds coexist in multi-layered situations, the CRE will depend on the optical properties of the two layers and their geometric locations within the atmosphere; the later controlling their temperature and the extent of absorbing gases above, below and between the cloud layers. Hence, the longwave (LW) or shortwave (SW) CRE due to a 2-layered cloud system cannot simply be expected to equal the corresponding CRE due to the 'effective' single-layered ice cloud with CTP and effective emissivity from a 1-layered $CO_2$-slicing solution. Thus, the accurate representation of the macrophysical and optical properties of both cloud layers in a scene is likely needed for accurate estimation of CRE in radiative transfer simulations. As a result, the accuracies of the MM_CTH method in determining macrophysical and optical cloud properties in 2-layered systems (Section 4.1) are expected to improve our estimates of modeled CRE for 2-layered systems. Here, we demonstrate this improvement due to the implementation of MM_CTH. We do this simply by estimating the impact of the 1-layer $CO_2$-slicing CTP and effective emissivity biases on simulated TOA upwelling and surface downwelling LW CRE. The impact of single-layer retrievals are ostensibly significant for shortwave (SW) CRE as well. Here, we do not study the SW CRE bias as that would be strongly dependent on multiple factors beyond layer-averaged properties (e.g., ice/water single-scattering properties and sun-satellite geometry), which would be beyond a concise explanation for the simple demonstration we are aiming for.

To estimate the LW impact of 1-layered $CO_2$-slicing retrievals applied to a 2-layered cloud system, we run radiative transfer simulations for different combinations of high and low cloud CTP and high cloud effective emissivity. In each of these cases, we calculate TOA upwelling and surface downwelling LW CRE for both the 'True' 2-layered cloud configuration (that we prescribe) and the 'Effective' single-layered ice cloud parameters (from a 1-layered $CO_2$-slicing retrieval). We define the CRE bias resulting from the application of a 1-layered $CO_2$-slicing as the difference between the 'True' CRE and 'Effective' CRE, defined as follows. 'True' LW CRE is defined as the difference between cloudy and clear-sky LW atmospheric radiative fluxes calculated using our pre-defined parameters for higher ice and lower water cloud properties. However, after the application of a 1-layered $CO_2$-slicing retrieval, we retrieve a single ice cloud layer at a lower altitude than the true altitude of the upper layer (Sections 3.2.1 and 4.1), along with its effective emissivity that is larger than its true emissivity (Section 4.1). We then use this retrieved 1-layer CTP and effective emissivity to calculate the LW CRE and compare it to the true LW CRE to assess the LW CRE bias. Further details of the radiative transfer simulations are in Text S2 of Supporting Information, which are for thin cirrus overlying a lower liquid water cloud that is opaque in the infrared. Figure 5 shows the variation of the surface and TOA LW CRE bias with true high and low cloud CTP and high cloud effective emissivity.

The left panels of Fig. 5 shows that the TOA LW CRE bias is sensitive to both the cloud macrophysics and high-cloud emissivity, which the true LW CRE is also sensitive too. The absolute value of the bias decreases with increasing effective emissivity of the upper cloud. As shown in Sections 3.2.1 and 4.1, applying a 1-layered $CO_2$-slicing retrieval on a 2-layered system results in overestimations in CTP and $A_c\epsilon_c$ for the upper-cloud layer. Since the retrieved cloud is lower in altitude, hence warmer, and more opaque in the infrared, the resultant top-of-atmosphere

LW CRE bias is negative, as shown in Figure 5, with the largest absolute bias (~40 $Wm^{-2}$) occurring for thin clouds near the tropopause overlying low altitude clouds.

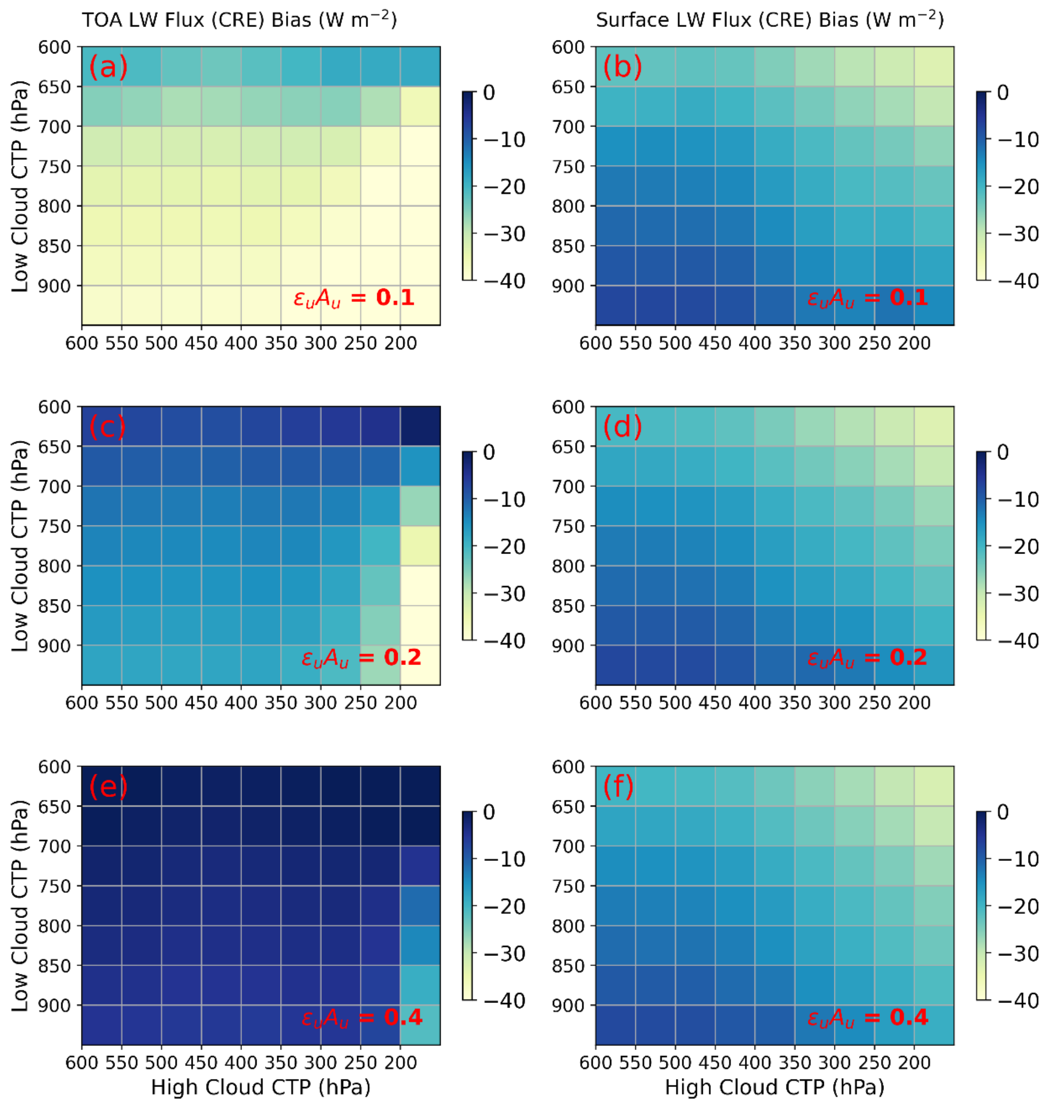


*Figure 5. Variation of top-of-atmosphere (left panels) and surface (right panels) LW Flux (CRE) bias ($W m^{-2}$) with variations in high and low CTP, due to a single-layered $CO_2$-slicing retrieval on a 2-layer scene. The atmosphere and surface properties are set up similar to Figure 1. CRE bias is defined as true minus modeled LW CRE. High Cloud Effective Emissivity is taken to be 0.1 (top panels), 0.2 (middle panels) and 0.4 (bottom panels).*

The right panels of Fig. 5 show the surface LW CRE bias is strongly sensitive to cloud macrophysics but less sensitive to high-cloud emissivity. Unlike the TOA, the true LW CRE at the surface is dependent only on the height of the low cloud because its LW emissivity is one in our simulations. Thus, in order to achieve the little differences that we see between Fig. 5(b), (d) and (f), the surface LW CRE calculated using the 1-layer $CO_2$-slicing solution must also be somewhat insensitive to the effective emissivity of the upper cloud. This occurs because the 1-layer $CO_2$-slicing solution produces a larger CTP bias, hence warmer cloud, for clouds with smaller emissivity compared to clouds with larger emissivity. Thus, changes in high cloud effective emissivity leads to competing changes in the resultant 1-layered retrieval (cloud temperature versus emissivity), thus impacting surface LW CRE bias only weakly. Thus, it is the heights of the two cloud layers that have the largest effect on the LW CRE bias, with absolute values of the bias being largest (~30 $Wm^{-2}$) for high tropospheric clouds overlying mid-level clouds.

Based on these findings, application of the MM_CTH algorithm is expected to provide improvements in modeled LW radiative fluxes that are of a similar order of magnitude (~10 W $m^{-2}$) to the CRE biases calculated here. These improvements to modeled radiative fluxes will be helpful when estimating, for example, the surface and atmospheric radiation budgets based on retrieved cloud properties [e.g., Kato et al. (2018)]. They may also provide a set of cloud properties that have variability that is more consistent with the variability in Earth's radiation budget, thereby providing improved benchmarks for the evaluation of climate models.

## 6. *Conclusions*

Thin cirrus cloud overlying low clouds constitute >80% of multi-layered clouds globally (multi-layered clouds themselves constitute ~30% of all cloud cover) (Wang & Dessler, 2006; Oreopoulos et al., 2017; Hong and Di Girolamo 2020). For 2-layered scenes, MODIS underestimates top-layer CTH by >1 km as the $CO_2$-slicing technique converges at a higher CTP solution, when an optically thin cirrus is present. As a result, MODIS produces more midlevel CTH than MISR and MISR-MODIS CTH differences have generally low absolute values (Naud et al., 2007; Mitra et al., 2021). However, MISR often retrieves the lower cloud height in a majority (>80%) of such 2-layered cases, provided the top-layer optical depth <~0.4 (Mitra et. al, 2021) In this study, we have developed an algorithm to retrieve accurate high-cloud properties for 2-layered cloud systems, named the *MISR-MODIS Fusion Product for Cloud-Top Height (MM_CTH)*. MM_CTH used a modified version of the standard MODIS $CO_2$-slicing algorithm (of the Collection 6.1 MOD06 product), using accurate MISR low-cloud CTH retrievals as an input to account for the presence of the lower cloud in multi-layer scenes. Using collocated ISS-CATS as a reference, we validate the MM_CTH retrievals to find a ~90% reduction in cirrus CTP bias over MOD06. This improvement to CTP accuracy propagates to ~75% improvements in accuracy for cirrus CTH and effective emissivity over the standard MOD06 products. The MM_CTH algorithm also allows us to retrieve lidar-like distributions of high cloud macrophysics (Figure 2b and 2d) and optical properties (Figure 3) in 2-layer cloud systems from passive sensors. Table 1 summarizes the results of the validation (Section 4.1) of $CO_2$-slicing CTP, CTH and thermal IR $A_c\epsilon_c$ (against CATS), and the distributions of CATS, MOD06 and MM_CTH CTP, CTH and $A_c\epsilon_c$.

| **Data Source** | **Mean Errors (with respect to CATS)** | | | **Net Distribution for High Clouds** | | |
|---|---|---|---|---|---|---|
| | **CTP (hPa)** | **CTH (km)** | $A_c\epsilon_c$ | **CTP (hPa)** | **CTH (km)** | $A_c\epsilon_c$ |
| **MOD06** | 65±85 | -1.6±2.3 | 0.4±0.3 | 300±85 | 9.7±2.3 | 0.5±0.3 |
| **MM_CTH** | 5±80 | -0.4±2.4 | 0.1±0.2 | 235±70 | 11.2±2.0 | 0.2±0.2 |
| **CATS** | N/A | N/A | N/A | 225±80 | 11.7±2.5 | 0.1±0.2 |

*Table 1. Summary of mean errors in $CO_2$-slicing CTP, CTH and effective emissivity for MOD06 and MM_CTH with respect to CATS and the mean value of the retrieved distributions of CTP, CTH and effective emissivity from MOD06, MM_CTH and CATS.*

We also performed a detailed error budget analysis using CATS high cloud retrievals as reference. CATS high cloud retrievals, ERA5 modeling error estimates, and estimates of MISR CTH and MISR, MODIS, CATS geo-collocation errors from Mitra et al., (2021) are used to model the systematic and random sources of CTP error, which are then compared against empirical estimates of errors (from comparison with CATS). 78% of all observed errors were found to be within theoretical limits (i.e., 95% CI), when non-opacity of low-cloud properties (stemming primarily from sub-pixel clouds) are neglected. However, when the sub-pixel nature of low-cloud is accounted for, up to 88% of observed MM_CTH error estimates fall within the limits of 95% CI – thus providing a near-closure of the MM_CTH error budget. The lack of a truth dataset for low-cloud cloud fraction and emissivity, uncertainties in prescribed surface emissivity, inaccuracies in MODIS cloud phase detection and the assumption in $CO_2$-slicing technique that ice-cloud effective emissivities in closely spaced IR channels are equal could potentially lead to the existence of the 7% outlier pixels. Since the benefit of including an estimate of sub-pixel (i.e., within a 1-km MODIS pixel) low-altitude cloud fraction is significant, it is recommended that MISR's Stereoscopic Derived Cloud Mask (SDCM; Mueller et al. (2013)) be reported at the native resolution of MISR, i.e. 275 m, rather than its current resolution of 1.1 km.

We demonstrated that the improvement in high cloud properties from the MM_CTH algorithm may be highly relevant in studies involving Earth's radiation budget. In 2-layered cloud systems, our results show improved estimates of modeled atmospheric fluxes (demonstrated for TOA and surface LW CRE in Figure 5) by ~5 to 40 W $m^{-2}$, depending on the 2-layered properties, when using MM_CTH retrievals rather than the standard single-layer $CO_2$-slicing retrievals. Thus, our algorithm could provide a climatology of CTH and high-cloud optical properties that is more consistent with the fluctuations in the Earth's radiation budget than corresponding estimates from standard MOD06 retrievals for multi-layered scenes.

Although this current study is concerned with introducing the pixel-level MM_CTH algorithm and its validation and error budget analysis, we would like to stress its future importance to broader climate science, especially in leveraging the 22-year-long stable Terra record to study long-term climate-scale cloud responses, especially for high cloud populations. Of the many cloud responses to anthropogenic forcing predicted by models, the highest confidence is associated with rising CTHs (Boucher et al. 2013). Rising CTH is predicted to be the first signal of forced change that will emerge above natural variability (Chepfer et al., 2014; Winker et al., 2017). For example, simulations of a uniform 21$^{st}$ century 4K warming had predicted the increase in high cloud amounts by ~5-15%, along with ~25 m/year increase in mean tropical high CTH (Chepfer et al., 2014). In fact, there have been non-significant detection of the expected rising patterns in global high cloud amounts from passive sensors (Norris et al., 2016; Aerenson et al., 2022). For confident detection of such trends, however, we need stable multi-decadal observations (subject to robust uncertainty analysis) of cloud vertical distribution, globally (Shea et al., 2017). While active sensors capable of vertically resolving cloud layers like lidars might seem ideal, the emergence of such trends from lidars are thwarted by their short lifetimes and lack of swath coverage. Hence, multidecadal passive sensor records from stable-orbit satellites like Terra are still the best suited for such a task.

However, as demonstrated in Section 1, both stereoscopic and multi-spectral retrievals of cloud macrophysics suffer from issues of sensitivity to different cloud types and accuracy. MISR stereo misses a majority of cirrus in 2-layered cases. On the other hand, unless the cirrus is very thin (OD << 1), MODIS IR channels detect cirrus emission above the channels' noise levels, but it is the restrictive choice of a 1-layer solution (in the MODIS forward model) that leads to the misrepresentation of cirrus properties, including its retrieved emissivity. Left unchecked, it would be difficult to impossible to decouple long-term changes in high cloud heights and emissivity from true changes in low cloud heights and amount using MODIS data alone. Similarly, it would be difficult to impossible to decouple long-term changes in low cloud heights and amounts from true changes in high cloud amount and optical depths from MISR data alone. MM_CTH is a means to tackle these problems as it can provide lidar-like distributions of high cloud properties over a passive sensor swath (the MISR swath) over the 22-year stable-orbit satellite record of Terra.

Due to its unmatched stability and longevity, the Terra record will remain a unique climate record of global cloud macro-physical and optical properties between 2000-2022. We are therefore left with the goal to ensure that the Terra record produces cloud products with well-characterized uncertainties for future studies on the Earth's climate. Towards this goal, we strongly recommend that the pixel-level MM_CTH algorithm introduced here be scaled to a fully operational product over the entire Terra record for public dissemination.

## 7. *Acknowledgements, Software and Data Sources*

This research was supported under MISR project contract 147871 with the Jet Propulsion Laboratory, California Institute of Technology. Partial support from the NASA ACCESS program under contract NNX16AMO7A is also acknowledged. The Collection 6.1 MODIS Level 2 Clouds Software modified to create the MM_CTH software was downloaded from the NASA Goddard Space Flight Center MODIS Adaptive Processing System (MODAPS) website (https://modaps.modaps.eosdis.nasa.gov/software/MODIS/AM1M/PGE06/Collection61/). The MISR data was downloaded from NASA Langley Research Center Atmospheric Sciences Data Center (https://opendap.larc.nasa.gov/opendap/MISR/MIL2TCSP.001/). The MODIS data were obtained through the Level 1 and Atmosphere Archive and Distribution System of NASA Goddard Space Flight Center (https://ladsweb.modaps.eosdis.nasa.gov/archive/allData/61/). The CATS data was downloaded from the NASA Langley Research Center's ASDC DAAC (https://opendap.larc.nasa.gov/opendap/CATS/). We are thankful to the NASA MODIS, MISR and CATS teams for supplying the documentation and tools, including the MISR toolkit (https://nasa.github.io/MISR-Toolkit/html/index.html). All ERA5 Reanalyses are downloaded through the European Center for Medium-Range Weather Forecast (ECMWF) Climate Data Store (CDS) website (https://cds.climate.copernicus.eu/cdsapp#!/home). The geoid data used in this study was downloaded from the National Geospatial-Intelligence Agency (NGA) WGS84 website (https://earth-info.nga.mil/index.php?dir=wgs84&action=wgs84). Data were stored and computations were conducted on the computing infrastructure managed by the University of Illinois at Urbana-Champaign's School of Earth, Society, and Environment (SESE).

## 8. *References*

Aerenson, T., Marchand, R., Chepfer, H., & Medeiros, B. (2022). When Will MISR Detect Rising High Clouds? Journal of Geophysical Research: Atmospheres, 127(2), e2021JD035865. https://doi.org/10.1029/2021JD035865

Anderson, G. P., Clough, S. A., Kneizys, F. X., Chetwynd, J. H., & Shettle, E. P. (1986). AFGL Atmospheric Constituent Profiles (0.120km). AIR FORCE GEOPHYSICS LAB HANSCOM AFB MA. Retrieved from https://apps.dtic.mil/sti/citations/ADA175173

Athreyas, K.N., Gunawan, E., & Tay, B. K. (2020). Estimation of vertical structure of latent heat generated in thunderstorms using CloudSat radar. Meteorological Applications, 27(2), e1902. https://doi.org/10.1002/met.1902

Baum, Bryan A., & Wielicki, B. A. (1994). Cirrus Cloud Retrieval Using Infrared Sounding Data: Multilevel Cloud Errors. Journal of Applied Meteorology and Climatology, 33(1), 107–117. https://doi.org/10.1175/1520-0450(1994)033<0107:CCRUIS>2.0.CO;2

Baum, Bryan A., Menzel, W. P., Frey, R. A., Tobin, D. C., Holz, R. E., Ackerman, S. A., et al. (2012). MODIS cloud-top property refinements for collection 6. Journal of Applied Meteorology and Climatology, 51(6), 1145–1163. https://doi.org/10.1175/JAMC-D-11-0203.1

Baum, Bryan A., Yang, P., Heymsfield, A. J., Bansemer, A., Cole, B. H., Merrelli, A., et al. (2014). Ice cloud single-scattering property models with the full phase matrix at wavelengths from 0.2 to 100µm. Journal of Quantitative Spectroscopy and Radiative Transfer, 146, 123–139. https://doi.org/10.1016/j.jqsrt.2014.02.029

Bouali, M., & Ladjal, S. (2011). Toward Optimal Destriping of MODIS Data Using a Unidirectional Variational Model. IEEE Transactions on Geoscience and Remote Sensing, 49(8), 2924–2935. https://doi.org/10.1109/TGRS.2011.2119399

Boucher, O., D. Randall, P. Artaxo, C. Bretherton, G. Feingold, P. Forster, V.-M. Kerminen, Y. Kondo, H. Liao, U. Lohmann, P. Rasch, S.K. Satheesh, S. Sherwood, B. Stevens and X.Y. Zhang, 2013: Clouds and Aerosols. In: Climate Change 2013: The Physical Sc, U. (2013). IPCC Ch 7: Clouds and Aerosols. https://doi.org/10.1017/CBO9781107415324.016

Cesana, G., Waliser, D. E., Henderson, D., L'Ecuyer, T. S., Jiang, X., & Li, J.-L. F. (2019). The Vertical Structure of Radiative Heating Rates: A Multimodel Evaluation Using A-Train Satellite Observations. Journal of Climate, 32(5), 1573–1590. https://doi.org/10.1175/JCLI-D-17-0136.1

Chepfer, H., Noel, V., Winker, D., & Chiriaco, M. (2014). Where and when will we observe cloud changes due to climate warming? Geophysical Research Letters, 41(23), 8387–8395. https://doi.org/10.1002/2014GL061792

Derber, J. C., Parrish, D. F., & Lord, S. J. (1991). The New Global Operational Analysis System at the National Meteorological Center. Weather and Forecasting, 6(4), 538–547. https://doi.org/10.1175/1520-0434(1991)006<0538:TNGOAS>2.0.CO;2

Fu, Q., & Liou, K. N. (1992). On the Correlated k-Distribution Method for Radiative Transfer in Nonhomogeneous Atmospheres. Journal of the Atmospheric Sciences, 49(22), 2139–2156. https://doi.org/10.1175/1520-0469(1992)049<2139:OTCDMF>2.0.CO;2

Graham, R. M., Hudson, S. R., & Maturilli, M. (2019). Improved Performance of ERA5 in Arctic Gateway Relative to Four Global Atmospheric Reanalyses. Geophysical Research Letters, 46(11), 6138–6147. https://doi.org/10.1029/2019GL082781

Hannon, S. E., Strow, L. L., & McMillan, W. W. (1996). Atmospheric infrared fast transmittance models: a comparison of two approaches. In Optical Spectroscopic Techniques and

Instrumentation for Atmospheric and Space Research II (Vol. 2830, pp. 94–105). SPIE. https://doi.org/10.1117/12.256106

Hersbach, H., Bell, B., Berrisford, P., Hirahara, S., Horányi, A., Muñoz-Sabater, J., et al. (2020). The ERA5 global reanalysis. Quarterly Journal of the Royal Meteorological Society, 146(730), 1999–2049. https://doi.org/10.1002/qj.3803

Hong, Y., & Di Girolamo, L. (2020). Cloud phase characteristics over Southeast Asia from A-Train satellite observations. Atmospheric Chemistry and Physics, 20(13), 8267–8291. https://doi.org/10.5194/acp-20-8267-2020

Hu, Y. X., & Stamnes, K. (1993). An Accurate Parameterization of the Radiative Properties of Water Clouds Suitable for Use in Climate Models. Journal of Climate, 6(4), 728–742. https://doi.org/10.1175/1520-0442(1993)006<0728:AAPOTR>2.0.CO;2

Joiner, J., Vasilkov, A. P., Bhartia, P. K., Wind, G., Platnick, S., & Menzel, W. P. (2010). Detection of multi-layer and vertically-extended clouds using A-train sensors. Atmospheric Measurement Techniques, 3(1), 233–247. https://doi.org/10.5194/amt-3-233-2010

Kang, H., Choi, Y.-S., Hwang, J., & Kim, H.-S. (2020). On the cloud radiative effect for tropical high clouds overlying low clouds. Geoscience Letters, 7(1), 7. https://doi.org/10.1186/s40562-020-00156-6

Kato, S., Rose, F. G., Rutan, D. A., Thorsen, T. J., Loeb, N. G., Doelling, D. R., Huang, X., Smith, W. L., Su, W., and Ham, S. (2018). Surface Irradiances of Edition 4.0 Clouds and the Earth's Radiant Energy System (CERES) Energy Balanced and Filled (EBAF) Data Product. Journal of Climate 31(11), 4501-4527. https://doi.org/10.1175/JCLI-D-17-0523.1

L'Ecuyer, T. S., Hang, Y., Matus, A. V., & Wang, Z. (2019). Reassessing the Effect of Cloud Type on Earth's Energy Balance in the Age of Active Spaceborne Observations. Part I: Top of Atmosphere and Surface. Journal of Climate, 32(19), 6197–6217. https://doi.org/10.1175/JCLI-D-18-0753.1

Li, J., Yi, Y., Minnis, P., Huang, J., Yan, H., Ma, Y., et al. (2011). Radiative effect differences between multi-layered and single-layer clouds derived from CERES, CALIPSO, and CloudSat data. Journal of Quantitative Spectroscopy and Radiative Transfer, 112(2), 361–375. https://doi.org/10.1016/j.jqsrt.2010.10.006

Li, Y., Thompson, D. W. J., & Bony, S. (2015). The Influence of Atmospheric Cloud Radiative Effects on the Large-Scale Atmospheric Circulation. Journal of Climate, 28(18), 7263–7278. https://doi.org/10.1175/JCLI-D-14-00825.1

Mace, G. G., & Berry, E. (2017). Using Active Remote Sensing to Evaluate Cloud-Climate Feedbacks: a Review and a Look to the Future. Current Climate Change Reports. Springer. https://doi.org/10.1007/s40641-017-0067-9

Marchand, R., Ackerman, T., Smyth, M., & Rossow, W. B. (2010). A review of cloud top height and optical depth histograms from MISR, ISCCP, and MODIS. Journal of Geophysical Research: Atmospheres, 115(D16). https://doi.org/10.1029/2009JD013422

Marchant, B., Platnick, S., Meyer, K., Arnold, G. T., & Riedi, J. (2016). MODIS Collection 6 shortwave-derived cloud phase classification algorithm and comparisons with CALIOP.

Atmospheric Measurement Techniques, 9(4), 1587–1599. https://doi.org/10.5194/amt-9-1587-2016

Mayer, B., & Kylling, A. (2005). Technical note: The libRadtran software package for radiative transfer calculations - description and examples of use. Atmospheric Chemistry and Physics, 5(7), 1855–1877. https://doi.org/10.5194/acp-5-1855-2005

McFarlane, N. (2011). Parameterizations: representing key processes in climate models without resolving them. WIREs Climate Change, 2(4), 482–497. https://doi.org/10.1002/wcc.122

McFarlane, S. A., Mather, J. H., Ackerman, T. P., & Liu, Z. (2008). Effect of clouds on the calculated vertical distribution of shortwave absorption in the tropics. Journal of Geophysical Research: Atmospheres, 113(D18). https://doi.org/10.1029/2008JD009791

McGill, M. J., Yorks, J. E., Scott, V. S., Kupchock, A. W., & Selmer, P. A. (2015). The Cloud-Aerosol Transport System (CATS): a technology demonstration on the International Space Station. In Lidar Remote Sensing for Environmental Monitoring XV (Vol. 9612, pp. 34–39). SPIE. https://doi.org/10.1117/12.2190841

Menzel, W. P., Frey, R. A., Zhang, H., Wylie, D. P., Moeller, C. C., Holz, R. E., et al. (2008). MODIS Global Cloud-Top Pressure and Amount Estimation: Algorithm Description and Results. Journal of Applied Meteorology and Climatology, 47(4), 1175–1198. https://doi.org/10.1175/2007JAMC1705.1

Menzel, W. P., R. A. Frey, and B. A. Baum (2015), Cloud Top Properties and Cloud Phase Algorithm Theoretical Basis Document Collection 006 Update. Available at https://atmosphere-imager.gsfc.nasa.gov/sites/default/files/ModAtmo/MOD06-ATBD_2015_05_01_1.pdf

Minnis, P., K-N. Liou, and Y. Takano (1993). Inference of cirrus cloud properties using satellite-observed visible and infrared radiances. Part I: Parameterization of radiance field. Journal of Atmospheric Sciences, 50**,** 1279–1304. https://doi.org/10.1175/1520-0469(1993)050<1279:IOCCPU>2.0.CO;2

Mitra, A., Di Girolamo, L., Hong, Y., Zhan, Y., & Mueller, K. J. (2021). Assessment and Error Analysis of Terra-MODIS and MISR Cloud-Top Heights Through Comparison With ISS-CATS Lidar. Journal of Geophysical Research: Atmospheres, 126(9), e2020JD034281. https://doi.org/10.1029/2020JD034281

Mueller, K., C. Moroney, V. Jovanovic, M.J. Garay, J.P. Muller, L. Di Girolamo, and R. Davies (2013). *MISR Level 2 Cloud Product Algorithm Theoretical Basis Document.* JPL Tech. Doc JPL D-73327, 61 pp.

Naud, C. M., Baum, B. A., Pavolonis, M., Heidinger, A., Frey, R., & Zhang, H. (2007). Comparison of MISR and MODIS cloud-top heights in the presence of cloud overlap. Remote Sensing of Environment, 107(1), 200–210. https://doi.org/10.1016/j.rse.2006.09.030

Norris, J. R., Allen, R. J., Evan, A. T., Zelinka, M. D., O'Dell, C. W., & Klein, S. A. (2016). Evidence for climate change in the satellite cloud record. Nature, 536(7614), 72–75. https://doi.org/10.1038/nature18273

Oreopoulos, L., Cho, N., & Lee, D. (2017). New insights about cloud vertical structure from CloudSat and CALIPSO observations. Journal of Geophysical Research: Atmospheres, 122(17), 9280–9300. https://doi.org/10.1002/2017JD026629

Platnick, S., Meyer, K. G., King, M. D., Wind, G., Amarasinghe, N., Marchant, B., et al. (2017). The MODIS Cloud Optical and Microphysical Products: Collection 6 Updates and Examples From Terra and Aqua. IEEE Transactions on Geoscience and Remote Sensing, 55(1), 502–525. https://doi.org/10.1109/TGRS.2016.2610522

Rajapakshe, C., Zhang, Z., Yorks, J. E., Yu, H., Tan, Q., Meyer, K., et al. (2017). Seasonally Transported Aerosol Layers over Southeast Atlantic are Closer to Underlying Clouds than Previously Reported. Geophysical Research Letters, Volume 44(Iss 11), 5818–5825. https://doi.org/10.1002/2017gl073559

Reynolds, R. W., Smith, T. M., Liu, C., Chelton, D. B., Casey, K. S., & Schlax, M. G. (2007). Daily High-Resolution-Blended Analyses for Sea Surface Temperature. Journal of Climate, 20(22), 5473–5496. https://doi.org/10.1175/2007JCLI1824.1

Rossow, W. B., and R. A. Schiffer, 1999: Advances in understanding clouds from ISCCP. *Bulletin of the American Meteorological Society*, 80**,** 2261–2287. https://doi.org/10.1175/1520-0477(1999)080<2261:AIUCFI>2.0.CO;2

Sassen, K., Wang, Z., & Liu, D. (2008). Global distribution of cirrus clouds from CloudSat/Cloud-Aerosol Lidar and Infrared Pathfinder Satellite Observations (CALIPSO) measurements. Journal of Geophysical Research: Atmospheres, 113(D8). https://doi.org/10.1029/2008JD009972

Seemann, S. W., Borbas, E. E., Knuteson, R. O., Stephenson, G. R., & Huang, H.-L. (2008). Development of a Global Infrared Land Surface Emissivity Database for Application to Clear Sky Sounding Retrievals from Multispectral Satellite Radiance Measurements. Journal of Applied Meteorology and Climatology, 47(1), 108–123. https://doi.org/10.1175/2007JAMC1590.1

Shea, Y. L., Wielicki, B. A., Sun-Mack, S., & Minnis, P. (2017). Quantifying the Dependence of Satellite Cloud Retrievals on Instrument Uncertainty. Journal of Climate, 30(17), 6959–6976. https://doi.org/10.1175/JCLI-D-16-0429.1

Tegtmeier, S., Anstey, J., Davis, S., Dragani, R., Harada, Y., Ivanciu, I., et al. (2020). Temperature and tropopause characteristics from reanalyses data in the tropical tropopause layer. Atmospheric Chemistry and Physics, 20(2), 753–770. https://doi.org/10.5194/acp-20-753-2020

Terai, C. R., Klein, S. A., & Zelinka, M. D. (2016). Constraining the low-cloud optical depth feedback at middle and high latitudes using satellite observations. Journal of Geophysical Research: Atmospheres, 121(16), 9696–9716. https://doi.org/10.1002/2016JD025233

Tetzner, D., Thomas, E., & Allen, C. (2019). A Validation of ERA5 Reanalysis Data in the Southern Antarctic Peninsula—Ellsworth Land Region, and Its Implications for Ice Core Studies. Geosciences, 9(7), 289. https://doi.org/10.3390/geosciences9070289

Voigt, A., Albern, N., Ceppi, P., Grise, K., Li, Y., & Medeiros, B. (2021). Clouds, radiation, and atmospheric circulation in the present-day climate and under climate change. WIREs Climate Change, 12(2), e694. https://doi.org/10.1002/wcc.694

Wang, L., & Dessler, A. E. (2006). Instantaneous cloud overlap statistics in the tropical area revealed by ICESat/GLAS data. Geophysical Research Letters, 33(15). https://doi.org/10.1029/2005GL024350

Weinreb, M. P., Xie, R., Lienesch, J. H., & D.S. Crosby. (1989). Destriping GOES images by matching empirical distribution functions. Remote Sensing of Environment, 29(2), 185–195. https://doi.org/10.1016/0034-4257(89)90026-6

Winker, D., Chepfer, H., Noel, V., & Cai, X. (2017). Observational Constraints on Cloud Feedbacks: The Role of Active Satellite Sensors. Surveys in Geophysics, 38(6), 1483–1508. https://doi.org/10.1007/s10712-017-9452-0

Yorks, J. E., McGill, M. J., Palm, S. P., Hlavka, D. L., Selmer, P. A., Nowottnick, E. P., et al. (2016). An overview of the CATS level 1 processing algorithms and data products. Geophysical Research Letters, 43(9), 4632–4639. https://doi.org/10.1002/2016GL068006

Yuan, T., & Oreopoulos, L. (2013). On the global character of overlap between low and high clouds. Geophysical Research Letters, 40(19), 5320–5326. https://doi.org/10.1002/grl.50871

Zhang, H., & Menzel, W. P. (2002). Improvement in thin cirrus retrievals using an emissivity-adjusted CO2 slicing algorithm. Journal of Geophysical Research: Atmospheres, 107(D17), AAC 2-1-AAC 2-11. https://doi.org/10.1029/2001JD001037

Zhao, G., & Di Girolamo, L. (2007). Statistics on the macrophysical properties of trade wind cumuli over the tropical western Atlantic. Journal of Geophysical Research: Atmospheres, 112(D10). https://doi.org/10.1029/2006JD007371

Zhou, C., Zelinka, M. D., Dessler, A. E., & Yang, P. (2013). An Analysis of the Short-Term Cloud Feedback Using MODIS Data. Journal of Climate, 26(13), 4803–4815. https://doi.org/10.1175/JCLI-D-12-00547.1